RSC Advances

PAPER

View Article Online
View Journal | View Issue

Cite this: *RSC Adv.*, 2024, **14**, 30116

Received 1st August 2024
Accepted 17th September 2024

DOI: 10.1039/d4ra05600k

rsc.li/rsc-advances

Detection of nitro-aromatics using C_5N_2 as an electrochemical sensor: a DFT approach†

Nabeela,[a] Muhammad Ali Hashmi,*[ab] Ahmad Nauman Shah Saqib,[a] Aqsa Kamran[a] and Ahmed Lakhani*[c]

Nitroaromatics impose severe health problems and threats to the environment. Therefore, the detection of such hazardous substances is essential to save the whole ecosystem. Herein, the C_5N_2 sheet is used as an electrochemical sensor for the detection of 1,3-dinitrobenzene (1,3-DNB), trinitrotoluene (TNT), and picric acid (PA) using the PBE0/def2SVP level of theory as implemented in Gaussian 16. The highest interaction energy was observed for the picric acid@C_5N_2 complex. The trend in interaction energies for the studied system is PA@C_5N_2 >TNT@C_5N_2 >1,3-DNB@C_5N_2. The studied systems were further analysed by qualitative and quantitative analyses to determine the interactions between the nitroaromatic analytes and the C_5N_2 sheet. Electronic properties of all analytes@C_5N_2 complexes have been examined by NBO, EDD, FMO and DOS analysis. QTAIM analysis depicts the stronger non-covalent interactions for the PA@C_5N_2, which shows consistency with interaction energy and NCI analysis. Furthermore, NBO and FMO analyses show that the C_5N_2 substrate exhibits high sensitivity and selectivity towards the picric acid compared to TNT and 1,3-DNB nitroaromatics. EDD and DOS analyses are in agreement with NBO and FMO analyses. Furthermore, the recovery time of the studied system has been computed to determine the efficiency of C_5N_2 material as an electrochemical sensor. Overall, the results show that carbon nitride can be a good sensor for the detection of nitroaromatics.

1 Introduction

In recent years, extensive use of explosives in defence systems has raised serious concerns as they have potential negative impacts on human health and the whole ecosystem.[1] Among these, nitroaromatics such as 1,3-dinitrobenzene (DNB), 2,4,6-trinitrophenol, also known as picric acid (PA), and trinitrotoluene (TNT), have been widely used due to their highly explosive nature. Besides, these nitroaromatics have also gained popularity in the synthetic industry, including pharmaceuticals, pigments, dyes, pesticides, wood preservatives, and rubber chemicals.[2–5] Release of these compounds, intentionally or unintentionally, contaminates the environment and deteriorates human health by causing problems such as skin irritation, cataracts, cancer, anaemia, cyanosis, and male infertility, damaging the liver, kidney, and blood cells in humans.[6–8] Therefore, detection of such toxic compounds is crucial to overcome their potential threats.

Various techniques such as HPLC, gas chromatography,[9] ion mobility spectrometry,[10–12] and capillary electrophoresis[13,14] have already been used for detection purposes. However, their non-specificity, difficulty in handling the instruments, pre-sample processes, expensive instrumentations, and portability hinder their applicability as detectors.[15,16] The demand for rapid, responsive, portable, and flexible detecting systems marked the electrochemical sensors as a potential alternative for efficient detection.[17]

Porous materials have gained significant importance as electrochemical sensors due to their exceptional sensing properties[18] and various 2D and 3D substrates have been evaluated both experimentally and theoretically for this purpose. Such substances include fullerene,[19] metal–organic frameworks (MOFs),[20] aluminium nitride,[21] silicon carbide,[22] ZnO nanotubes,[23] silver–graphene quantum dots,[24] metal-doped graphene,[25,26] and covalent organic frameworks.[27] In addition to these, graphene–polyaniline,[28] polyaniline/ZnO,[29] single-walled nanotubes,[30] multi-walled nanotubes,[31] polypyrrole,[32] and h-BN nanoclusters[33] have been used for detecting the chemical warfare agents (CWAs) including nitro explosives. Although these adsorbents are used to sense toxic agents, they lack certain characteristics, such as large surface area coupled with more active sites for adsorption, high porosity and reproducible results, required for the efficient performance of the adsorbents.[34]

---

[a] *Department of Chemistry, Division of Science & Technology, University of Education, Lahore, 54770, Pakistan. E-mail: muhammad.hashmi@ue.edu.pk*

[b] *School of Chemical and Physical Sciences, Victoria University of Wellington, Wellington, 6012, New Zealand*

[c] *Department of Biomedical and Health Sciences, Calumet College of St. Joseph, 2400, New York Ave, Whiting, IN, 46394, USA. E-mail: alakhani@ccsj.edu*

† Electronic supplementary information (ESI) available. See DOI: **https://doi.org/10.1039/d4ra05600k**

Recently, carbon nitride became the heart of sensors due to its specific surface area and highly porous and chemically stable structure. Moreover, the intrinsic bandgap of carbon nitride proves its efficacy as a catalyst in water-splitting reactions, carbon dioxide reduction reactions, and degradation of organic pollutants.[35,36] Numerous experimental and theoretical studies have been performed on the sensing capability of carbon nitride having different ratios of carbon and nitrogen, such as C_2N, C_3N_4, and C_4N nanoflakes.[37] These materials show excellent sensing performance in the detection of toxic agents containing ammonia, hydrogen sulphides,[38] pesticides,[39] nitrogen halides,[40] neurotoxin hydrazine derivatives,[41] CWAs,[42,43] and nitro-explosives.[44,45]

An innovative form of carbon nitride, *i.e.* C_5N_2, has not yet been explored for sensing. The C_5N_2 material is synthesised through a condensation reaction between 1,2,4,5-benzene tetramine and hexaketocyclohexane.[46,47] Theoretical studies showed that C_5N_2 is used as a catalyst to determine its stability and activity for the synthesis of hydrogen peroxide (H_2O_2).[48] Moreover, C_5N_2 is superior to the other carbon nitride forms due to its nanoporous crystalline structure with a narrow band gap (1.10 eV).[49] These findings motivated us to explore the sensing capability of the C_5N_2 toward the nitroaromatic compounds, *i.e.*, PA, 1,3-DNB and TNT. DFT calculations have been performed to determine the adsorption of the analytes on the C_5N_2 surface. The selectivity and sensitivity of the analytes on the C_5N_2 surface have been investigated by the FMO, NBO and DOS analyses. Furthermore, the nature of interactions is explored through the QTAIM and NCI analyses.

2 Computational methodology

Quantum chemistry computational calculations have been performed using Gaussian 16 B.01.[50] Structures of analystes, C_5N_2 and complexes have been modelled using Gauss View software.[51] Geometries of the substrate C_5N_2 and nitro-containing analytes were optimised at the PBE0-D3BJ/def2-SVP level of theory. PBE0 is a hybrid DFT functional, which outperforms the pure DFT approach in computing molecular structures and properties throughout the periodic table.[52] The literature has also backed the selection of PBE0 functional as it is widely applicable for molecular systems, providing accurate results for atomic energies, structural geometry, dissociation energies, and electronic and magnetic properties[53] and sensing interactions.[54] PBE0/def2XVP has been used for adsorption studies of CO_2,[55] metformin,[56] and different gases including H_2, N_2, CO, H_2S, NH_3, SO_2, and CH_4 [57] over graphitic carbon nitride and to study the non-covalent interactions between the decavanadate, arginine, and lysine side chains in proteins.[58] Similarly, PBE0 has also been studied with different basis set combinations to study Se-doped graphitic carbon nitride ($Se@gC_3N_4$) nanostructures used for the smart therapeutic delivery of zidovudine,[59] for the efficient sensing of glucose towards borophene,[53] functionalized carbon quantum dots for sensing curcumin,[60] and in studying the sensing of telomerase through semiconducting carbon nitrides.[61] In a study about adsorption behaviour for efficient sensing of melamine through $Mg_{12}O_{11}$–X nanostructured materials, different hybrid functionals have been employed, and PBE0 has been reported to be ranked at the top in describing the sensing interactions.[54] Considering the long-range non-covalent interactions, Grimme's empirical D3 correction[62] with Becke–Johnston damping (D3BJ)[63] has been applied in all calculations. Multiwfn (version 3.80)[64] and VMD software[65] have been used for qualitative and quantitative analyses. CYLview[66] has been employed to obtain high-resolution visualisation of modelled structures.

Analytes with different orientations on the C_5N_2 sheet have been optimised to obtain the lowest energy structure of the complexes. These optimised structures are further validated *via* the vibrational frequency analysis, ensuring they have no imaginary frequency. The interaction energies of analytes with the sheet have been calculated through the following formula:

$$\Delta E_{\text{int}} = [E_{\text{analyte@C}_5\text{N}_2} - (E_{\text{analyte}} + E_{\text{C}_5\text{N}_2})] \tag{1}$$

ΔE_{int} represents the interaction energy of the analyte@C_5N_2 substrate, whereas the energy of complex, analyte, and C_5N_2 sheet, respectively, are shown by the terms $E_{\text{analyte@C}_5\text{N}_2}$, E_{analyte}, and $E_{\text{C}_5\text{N}_2}$.

The interactions between the C_5N_2 substrate and the nitro analytes have been thoroughly analyzed using Non-Covalent Interactions (NCI) analysis. This method primarily utilizes electron density (ρ) and the Reduced Density Gradient (RDG) to probe these interactions. The RDG is calculated using the following equation:[67]

$$\text{RDG (s)} = \frac{1}{2(3\pi^2)^{\frac{1}{3}}}\frac{\nabla\rho}{\rho^{\frac{4}{3}}} \tag{2}$$

This equation indicates that the RDG value is inversely proportional to the electron density at a point. A higher electron density generally leads to a lower RDG value, suggesting a stronger potential for non-covalent bonding at that location.

Additionally, the electron density magnitude influences these non-covalent interactions' strength. In contrast, the interaction's specific nature—whether repulsive or attractive—is determined by the Laplacian of the electron density ($\nabla^2\rho$). The Laplacian is expressed as the sum of its three eigenvalues from the Hessian matrix of electron density:[24]

$$\nabla^2\rho = \lambda_1 + \lambda_2 + \lambda_3 \tag{3}$$

Among the eigenvalues derived from the Hessian matrix, the second eigenvalue (λ_2) is especially important for determining the nature of the interactions within the molecule. Specifically, a negative λ_2 indicates strong, attractive interactions, such as those seen in hydrogen bonds, which are critical for molecular stability and function. Conversely, a positive λ_2 points to repulsive interactions, which might indicate regions of molecular strain or steric clashes. Additionally, when λ_2 is near zero, it typically signifies the presence of weaker interactions, like van der Waals forces, which are essential for subtler molecular phenomena.

To visually capture and illustrate these different types of non-covalent interactions, we employ 2D RDG graphs and 3D iso-surfaces generated using Multiwfn Software (version 3.80).[64,68] These visualizations are color-coded to enhance understanding and interpretation: red represents repulsive interactions, blue denotes strong attractive interactions (notably hydrogen bonds), and green highlights the van der Waals interactions. This color-coding aids in quickly identifying the nature of interactions at a glance, providing an intuitive map of molecular interaction landscapes.[69]

Furthermore, Quantum Theory of Atoms in Molecules (QTAIM) analysis has been performed to recognise the intra-molecular and intermolecular interactions, particularly the non-covalent interactions.[70,71] The nature and strength of intermolecular interactions between the nitroaromatic analytes and C_5N_2 substrate are determined by the various topological parameters such as electron density (ρ), kinetic and potential energy density (G and V), total electron energy density (H), and Laplacian of the electron density ($\nabla^2\rho$), which exist at bond critical points (BCP) between nitroaromatic analytes and the substrate.[69]

$$H(r) = V(r) + G(r) \tag{4}$$

Generally, the values of potential energy density and kinetic energy density are always negative and positive, respectively. The sum of these two parameters (V and G) gives the total energy density (H). The values of H and $\nabla^2\rho$ depict the type of interactions either covalent or non-covalent. If the value is $H > 0 < \nabla^2\rho$, then it shows the non-covalent interactions, while covalent interactions are depicted by the $H < 0 > \nabla^2\rho$.[71,72] Electronic density values further specify the strength of non-covalent interactions. If the value of electronic density is greater than 0.1, then it indicates the electrostatic attractive forces, while the presence of van der Waals interactions is indicated by the value of electronic density lower than 0.1.[73]

In addition, the electronic properties of the analytes@C_5N_2 complexes have been determined at the same level of theory through frontier molecular orbital (FMO), electron density distribution (EDD), density of states (DOS) and natural bond orbital (NBO) analysis. The density of states validates the FMO analysis by better understanding the energy gap after the adsorption of analytes. EDD plots of electronic density were obtained using Chemcraft.[74] Moreover, NBO charges are confirmed by providing visual aids through EDD plots to understand charge transfer upon complexation.

3 Results and discussion

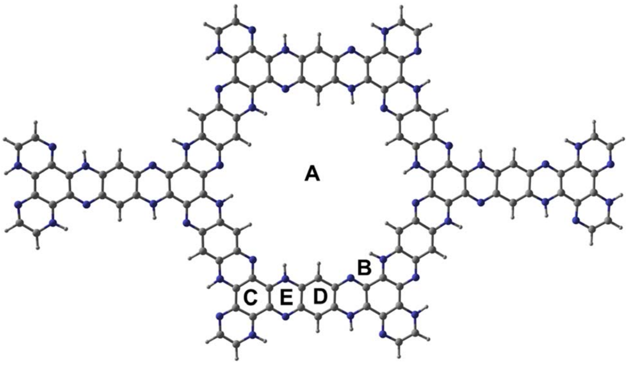

Fig. 1 Optimised geometry of C_5N_2 at PBE0-D3BJ/def2SVP with five binding sites *i.e.*, central cavity (A), triazine site (B), benzene ring (C), hydrogenated benzene ring (D) and pyrazine ring (E). Blue color shows the nitrogen atom, grey shows the carbon atom and greyish-white shows the hydrogen.

Fig. 1 shows the optimised structure of C_5N_2 used as an adsorbent. C_5N_2 sheet consists of five fused benzene rings, bridged by a pyrazine ring, consisting of four different kind of bonds, depending on the type of atoms and ring involved. The C–N bond length in the pyrazine ring is 1.36 Å whereas the bond length of three types of C–C bonds is 1.4 Å, 1.42 Å and 1.38 Å present in pyrazine, benzene and hydrogenated benzene rings, respectively. The analytes (1,3-DNB, TNT and PA) were placed on five possible binding sites with different orientations to get the most stable ones. Such sites are labelled as A (in the central cavity of the sheet), B (forming a triangle with nitrogen atoms at the edges), C (top of the benzene ring), D (top of the pyrazine ring) and E (top of hydrogenated benzene ring). Analytes were positioned with possible orientations on the mentioned sites of the C_5N_2 sheet to get the most stable geometry of the complex.

Among the possible orientations of the 1,3-DNB complex (see Fig. S1†), the most stable geometry occurred at the top of the pyrazine ring with an interaction energy of −23.21 kcal mole^{-1}. The benzene ring of the 1,3-DNB analyte was located on the site D while the two nitro groups were situated on the site B and E of the C_5N_2 surface, respectively. For the TNT@C_5N_2 complex, the analyte was placed in five possible orientations on the C_5N_2 sheet (see Fig. S3†). Among these, the most stable geometry was obtained with an interaction energy of −31.64 kcal mole^{-1} where the analyte was oriented in between the C and D sites of the surface. The oxygen of TNT formed a hydrogen bond with the hydrogen pyrazine ring of C_5N_2 substrate (2.49 Å). The interaction energies of the possible orientation of analytes at C_5N_2 are also presented in Table S1.† Stable geometries of 1,3-DNB@C_5N_2, TNT@C_5N_2 and PA@C_5N_2 have been shown in Fig. 2.

Among all the three complex systems, picric acid interacts strongly with the surface of the substrate. For PA@C_5N_2 complexes, the most stable geometry is obtained when the analyte is located on the top of the D site (pyrazine ring) with −34.37 kcal mole^{-1} of interaction energy. The other unstable optimized structures are presented in Fig. S2.† One of the reasons for such a high interaction energy is the formation of a hydrogen bond between the oxygen of picric acid and hydrogen of the pyrazine ring. The interaction energies of TNT@C_5N_2 and PA@C_5N_2 are stronger than those of the 1,3-DNB@C_5N_2 complex due to the presence of hydrogen bond formation between the analyte and the substrate. Trends in interaction energies for the considered complexes are PA@C_5N_2 > TNT@C_5N_2 > 1,3-DNB@C_5N_2. The interaction energies along

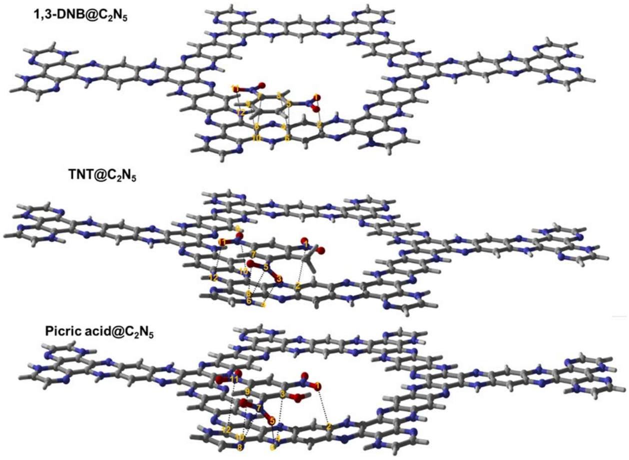

Fig. 2 The stable optimised structure of 1,3-DNB@C_5N_2, TNT@C_5N_2 and picric acid@C_5N_2 at PBE0-D3BJ/def2SVP level of theory. Interacting atoms of analytes and substrate have been shown by dotted lines.

with bond lengths of all three complex systems have been presented in Table 1.

3.1 Quantum theory of atoms in molecules analysis

The nature of intermolecular interactions in nitroaromatics@C_5N_2 complexes is analysed through the quantum theory of atoms in molecules (QTAIM) analysis. For the 1,3-DNB@C_5N_2 complex, seven BCPs with four C–C, one C–N, one C–O, and one N–O were identified between the 1,3-DNB and C_5N_2 substrate, as shown in Fig. 3. The value of Laplacian of electron density ranges from 0.019 to 0.033, signifying the non-covalent interactions, while electron density exhibits a value less than 0.1 (0.008 to 0.011), depicting the van der Waals interactions between the 1,3-DNB and C_5N_2 sheet. Additionally, the remaining topological parameter values, *i.e.*, H, G and V of 1,3-DNB@C_5N_2 also indicate the presence of non-covalent interactions (Table S2†). For the TNT@C_5N_2, eleven BCPs with two C–C, three C–N, two C–O, one C–H, one N–N, and two N–O were observed, as shown in Fig. 3. Topological parameters at the mentioned BCPs show non-covalent interactions between the TNT and C_5N_2 substrate. The values of Laplacian and electron density range from 0.023 to 0.037 and 0.007 to 0.014, respectively. The remaining topological parameters, *i.e.*, H, G and V of TNT@C_5N_2 also indicated the presence of non-covalent interactions (see Table S1†).

In the case of PA@C_5N_2, ten BCPs are obtained with one O–H, two C–O, three C–C, two C–N, one N–N, and one N–O, between the picric acid and substrate (see Fig. 3). The topological parameters of PA@C_5N_2 were similar to the TNT@C_5N_2 except for the one O–H BCP. For all the BCPs, values of Laplacian and electron density range from 0.023 to 0.033 and 0.005 to 0.012, respectively. These topological values were in good agreement with the non-covalent interactions, particularly the van der Waals interactions. The value of electron density was highest for BCPs between the C8 of the picric acid and C18 of the C_5N_2 surface which depicted the strong non-covalent interactions. The rest of topological parameters (H, G, V) also showed consistency with values of Laplacian and electron density as reported in Table 2.

Topological parameters for all considered complexes indicated the presence of non-covalent interaction between the analytes and the C_5N_2 substrate. Values of electron density and Laplacian for PA@C_5N_2 complexes showed van der Waals interactions along with hydrogen bond interactions. These QTAIM results are consistent with the interaction energies.

3.2 Non-covalent interaction analysis

The intermolecular interactions have been further characterised by the NCI analysis in the complexes of analytes–C_5N_2. It

Table 1 Interaction energies of all the complexes in kcal mol^{-1} along with bond length (Å) of interacting atoms of analytes and C_5N_2 substrate

Analyte@C_5N_2 sheet complex	Interacting atoms of analytes and C_5N_2	Bond lengths (Å)	Interaction energies (kcal mol^{-1})
PA@C_5N_2	N7–N8	3.05	−34.37
	O5–H6	2.67	
	C3–N4	3.06	
	C9–C10	2.99	
	N11–C12	3.06	
	O1–C2	3.01	
TNT@C_5N_2	N5–N6	2.91	−31.64
	C7–C8	2.92	
	O11–N12	3.03	
	N1–C2	3.09	
	O9–N10	3.15	
	O3–H4	2.49	
1,3-DNB@C_5N_2	C7–C8	3.17	−23.21
	C9–C10	3.09	
	C5–C6	3.11	
	C3–C4	3.15	
	O1–C2	2.99	
	O11–N12	3.01	

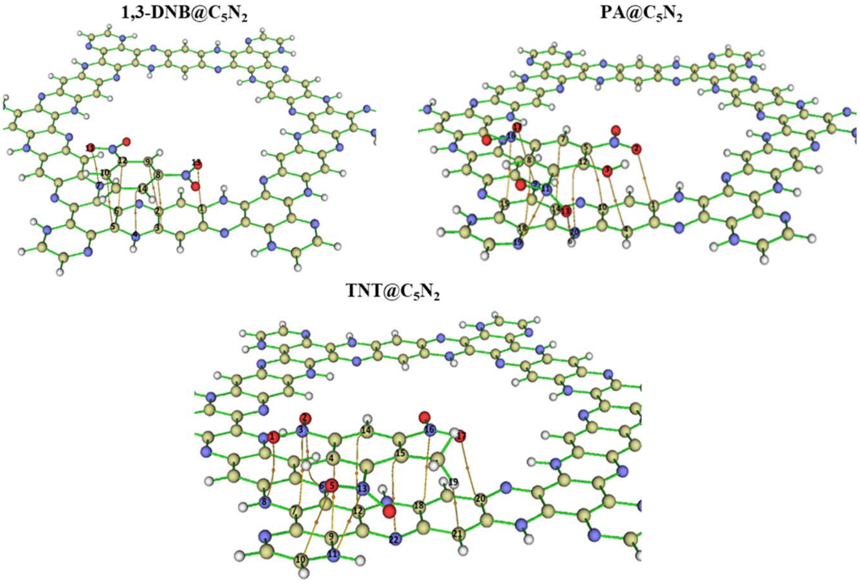

Fig. 3 Visual representation of BCPs *via* QTAIM analysis of the considered analytes@C$_5$N$_2$ complexes.

Table 2 QTAIM topological parameters for PA@C$_5$N$_2$. Topological parameters are ρ (electron density), $\nabla 2\rho$ (Laplacian of electron density), G (kinetic energy density), V (potential energy density) and H (total electron energy density)

Analyte–C$_5$N$_2$	$\nabla_2\rho$	ρ	$V(r)$	H	$G(r)$
PA@C$_5$N$_2$					
N11–N19	0.027	0.0082	−0.005	0.001	0.006
C8–C18	0.033	0.0121	−0.006	0.001	0.007
O2–C1	0.031	0.0101	−0.006	0.001	0.007
O13–H6	0.023	0.0055	−0.004	0.001	0.005
O17–N9	0.024	0.0069	−0.005	0.001	0.005
N16–C15	0.030	0.0085	−0.005	0.001	0.006
C12–N20	0.028	0.0099	−0.005	0.001	0.006
O3–C4	0.025	0.0084	−0.005	0.001	0.005
C7–C14	0.026	0.0091	−0.004	0.001	0.005
C5–C10	0.027	0.0096	−0.005	0.001	0.006

comprises of 2D RDG graph and 3D isosurfaces. Three color schemes have been used in 3D isosurface which describes the non-covalent interactions *i.e.*, blue, green and red for attractive, weak van der Waals, and dispersive interactions between the analytes and substrate. Similarly, the 2D RDG graph shows attractive interactions in the form of hydrogen bonding (blue spikes), repulsive force (red spikes) and weak van der Waals forces (green spikes). Whereas the size of a particular patch is directly related to the strength of interactions. The larger the size of a particular patch, the greater will be the strength of that interaction. Similarly, values of electron density on the *x*-axis vary directly with the nature of interactions between the analytes and the substrate.

In the 3D isosurface, the presence of green isosurface between the analytes (1,3-DNB, TNT and PA) and the C$_5$N$_2$ substrate confirms the weak van der Waals interactions consistent with the 2D RDG graph. Conversely, there is no hydrogen bond interaction between the analytes and substrate as revealed by the absence of clear blue patches.[75] However, dispersed bluish-green spots in the case of TNT@C$_5$N$_2$ and PA@C$_5$N$_2$ showed more van der Waals interactions. 2D RDG and 3D isosurface are presented in Fig. 4. Moreover, the presence of red spikes (0.01 to 0.03) in the 2D RDG graph represents the repulsive interaction that mostly exists between the atoms of aromatic rings of the C$_5$N$_2$ substrate, also depicted in the 3D isosurface.[76] In the case of picric acid@C$_5$N$_2$ complex, the green isosurface and spikes in 3D and 2D graphs respectively, are dense and wide as compared to 1,3-DNB and TNT complexes, reflecting more van der Waals interactions between the picric acid and C$_5$N$_2$ which is also consistent with the interaction energies and QTAIM topological results.

3.3 Electronic properties: FMO and DOS analysis

Electronic properties of the substrate upon complexation have been studied through FMO analysis. After the analytes' adsorption, the substrate's conductivity significantly changed, which influenced its sensing capability. FMO analysis for the considered analytes@C$_5$N$_2$ complexes has been performed. The energy values of HOMO, LUMO and their energy gaps have been reported in Table 3. Orbital density isosurface of all the analytes@complexes are shown in Fig. 5. Analysis shows that HOMO and LUMO values for pristine C$_5$N$_2$ substrate are −3.42 eV and −2.82 eV respectively, which results in an energy gap of 0.60 eV. The energy gap of the pristine C$_5$N$_2$ has been changed after complexation with the analytes (1,3-DNB, TNT and PA). HOMO and LUMO energy values of 1,3-DNB@C$_5$N$_2$ have been increased to −3.41 eV and −2.94 eV, respectively which results in decreased value of $E_{\mathrm{H-L}}$ gap (0.47 eV). After adsorption of TNT analytes upon C$_5$N$_2$, the HOMO–LUMO energy gap reduces to 0.46 eV similar to the 1,3-DNB@C$_5$N$_2$ complex. In this case, the

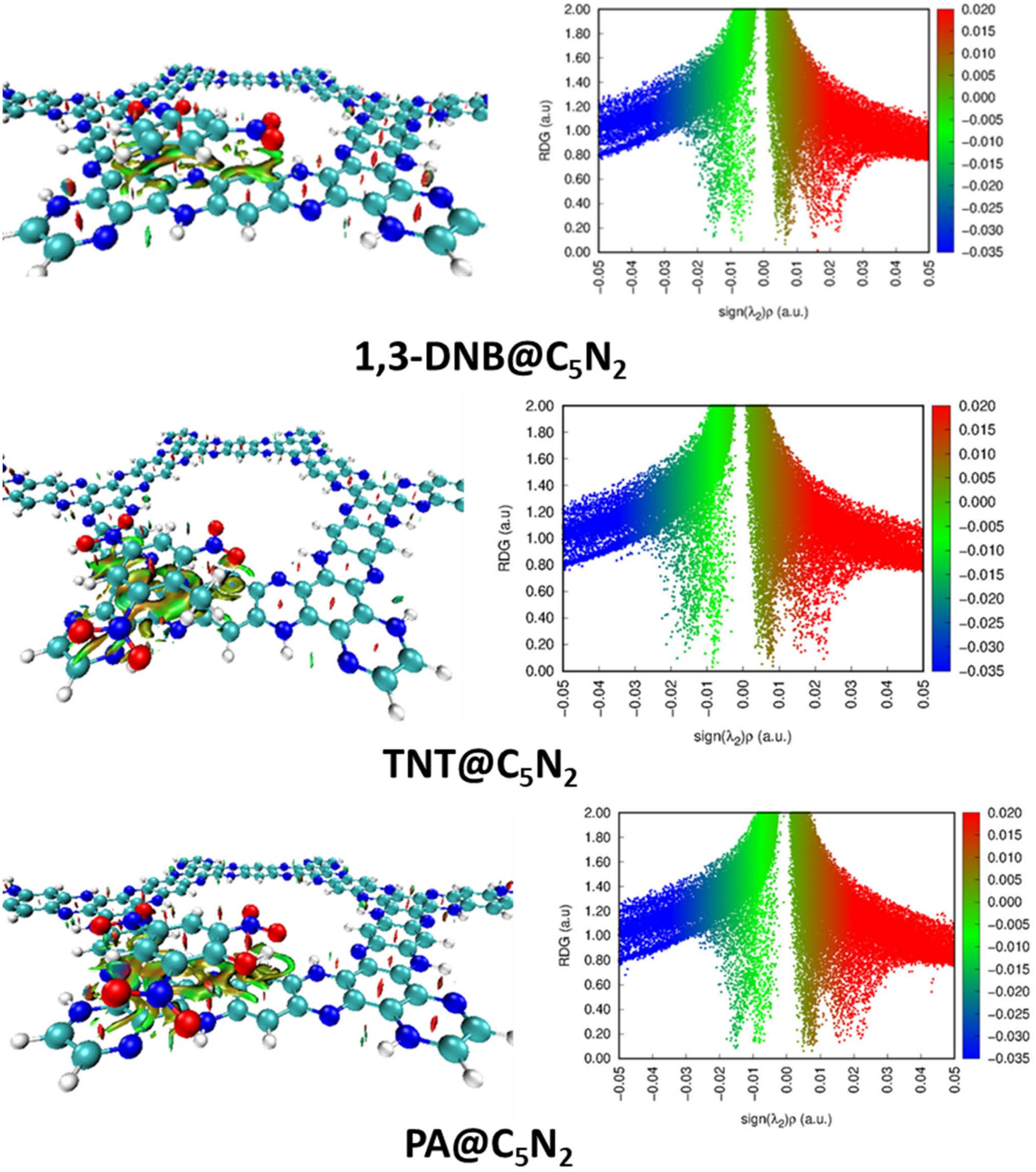

Fig. 4 3D isosurface and 2D RDG graph of nitroaromatics analytes@C_5N_2 complexes.

decrease in E_{H-L} gap is now attributed to the decreased value of both HOMO (−3.47 eV) and LUMO (−3.01 eV) as compared to the pristine C_5N_2 substrate. Among all the studied systems, a significant reduction in the HOMO–LUMO energy gap is observed in the case of PA@C_5N_2. The value of HOMO is reduced to −3.47 eV, comparable to the HOMO value of the pristine C_5N_2. However, pronounced shift in E_{H-L} is mainly due to the reduction in the value of LUMO (−3.10 eV). This noticeable reduction in energy gap (0.37 eV) results in excellent conductivity and sensitivity of C_5N_2 substrate towards the picric acid as compared to the other analytes (1,3-DNB and TNT).[77]

Table 3 HOMO–LUMO energies and their energy gap (eV) of all the three analytes–complexes and bare C_5N_2 sheet along with NBO results

Analyte@C_5N_2	Pristine C_5N_2	PA@C_5N_2	TNT@C_5N_2	1,3-DNB @C_5N_2
HOMO (eV)	−3.42	−3.47	−3.47	−3.41
LUMO (eV)	−2.82	−3.10	−3.01	−2.94
E_{H-L} gap (eV)	0.60	0.37	0.46	0.47
NBO charge (e^-)		−0.426	−0.406	−0.228

Orbital density patterns for considered analytes@C_5N_2 complexes obtained through FMO analysis are shown in Fig. 5. Orbital density distribution shows similar patterns in all three analytes@C_5N_2 complex systems. For all three systems (1,3-DNB@C_5N_2, TNT@C_5N_2, PA@C_5N_2), the HOMO isosurface lies entirely on the sheet depicting the transfer of charge density from the C_5N_2 surface after adsorption of analytes. The LUMO density orbital is found half on the analyte and half on the substrate which shows a significant reduction in the HOMO–LUMO energy gap. Among the 1,3-DNB@C_5N_2 and TNT@C_5N_2 complexes, PA@C_5N_2 shows larger orbitals density isosurface, depicting the major shift in electronic density between C_5N_2 and picric acid. This visual representation is analogous to the reduced HOMO–LUMO energy gap resulting in excellent sensitivity of picric acid toward the C_5N_2 as compared to the rest of the analytes.

Electronic properties of considered complexes are further executed by the DOS analysis. The spectra of DOS are plotted in Fig. 6 for a better understanding of interactions after adsorptions of analytes. Density of state spectra reveals that after adsorption of analytes, virtual orbitals are shifted more negatively, resulting in a reduced energy gap. In the DOS spectra, it is observed that HOMO appeared at −3.47 eV for PA@C_5N_2 and TNT@C_5N_2 as compared to pristine C_5N_2 sheet (−3.42 eV) while the LUMO virtual orbitals are shifted to −3.10 eV and −3.01 eV from −2.82 eV of C_5N_2, respectively. The formation of new orbitals of HOMO and LUMO results in a reduction of energy gap as compared to pristine substrate. A similar pattern is also observed for the 1,3-DNB@C_5N_2 complex. Among the studied systems, the more pronounced shift is observed for the PA@C_5N_2 system, thus lowering the energy gap. The shifting of orbitals and their peak intensities reflect the conductivity and sensitivity of C_5N_2 towards analytes, validating FMO results.[76]

3.4 NBO and EDD analysis

Natural bond orbital (NBO) analysis provides a deeper evaluation of the interaction mechanism by determining the amount of charge transfer between the nitroaromatic analytes and C_5N_2 substrate upon complexation. The NBO results of nitroaromatics@C_5N_2 complexes are presented in Table 3. The values of NBO charges are negative on the 1,3-DNB, TNT and PA in nitroaromatics@C_5N_2 complexes (presented in Table 3), which shows that charges are transferred from the sheet towards the nitroaromatics analytes. For the TNT@C_5N_2 complex, 0.406 *e* charge is shifted from the C_5N_2 substrate to TNT. Similarly, 0.426 *e* charge is being transferred from substrate to PA in case of PA@C_5N_2 complex while for 1,3-DNB@C_5N_2 complex, the amount of charge transferred from substrate to the analyte is only 0.208 *e*. From these results, it is deduced that PA extracted the highest amount of charge from the C_5N_2 substrate as compared to TNT and 1,3-DNB.[78]

Electron density difference (EDD) analysis helps to visualize the electronic density distribution among the nitroaromatics analytes and substrate upon complexation. The difference in the electronic density of the nitroaromatics@C_5N_2 complex and the sum of the electronic density of the nitroaromatic analytes and C_5N_2 substrate, taken separately, gives the EDD results.[44] The EDD plots are given in the Fig. 7. In EDD plots, the transfer of electronic density is depicted by the orange (electronic density accumulated region) and pink (electronic density depleted region) colored isosurface, at the interacting sites of nitroaromatics and C_5N_2 substrate. EDD results of 1,3-DNB@C_5N_2 and TNT@C_5N_2 show that nitroaromatics are mainly covered with orange isosurface, indicating the analytes withdraw electron density from C_5N_2 substrate. In the EDD plot

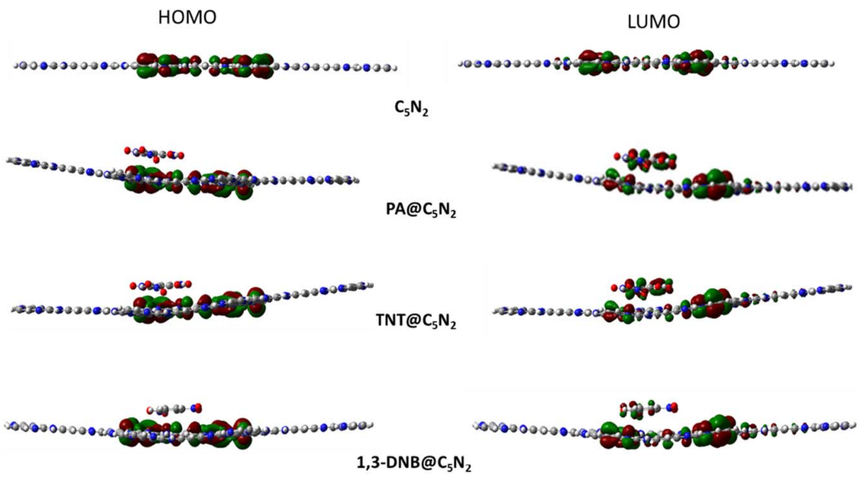

Fig. 5 HOMO–LUMO orbitals densities of the pristine C_5N_2, PA@C_5N_2, TNT @C_5N_2 and 1,3-DNB@C_5N_2.

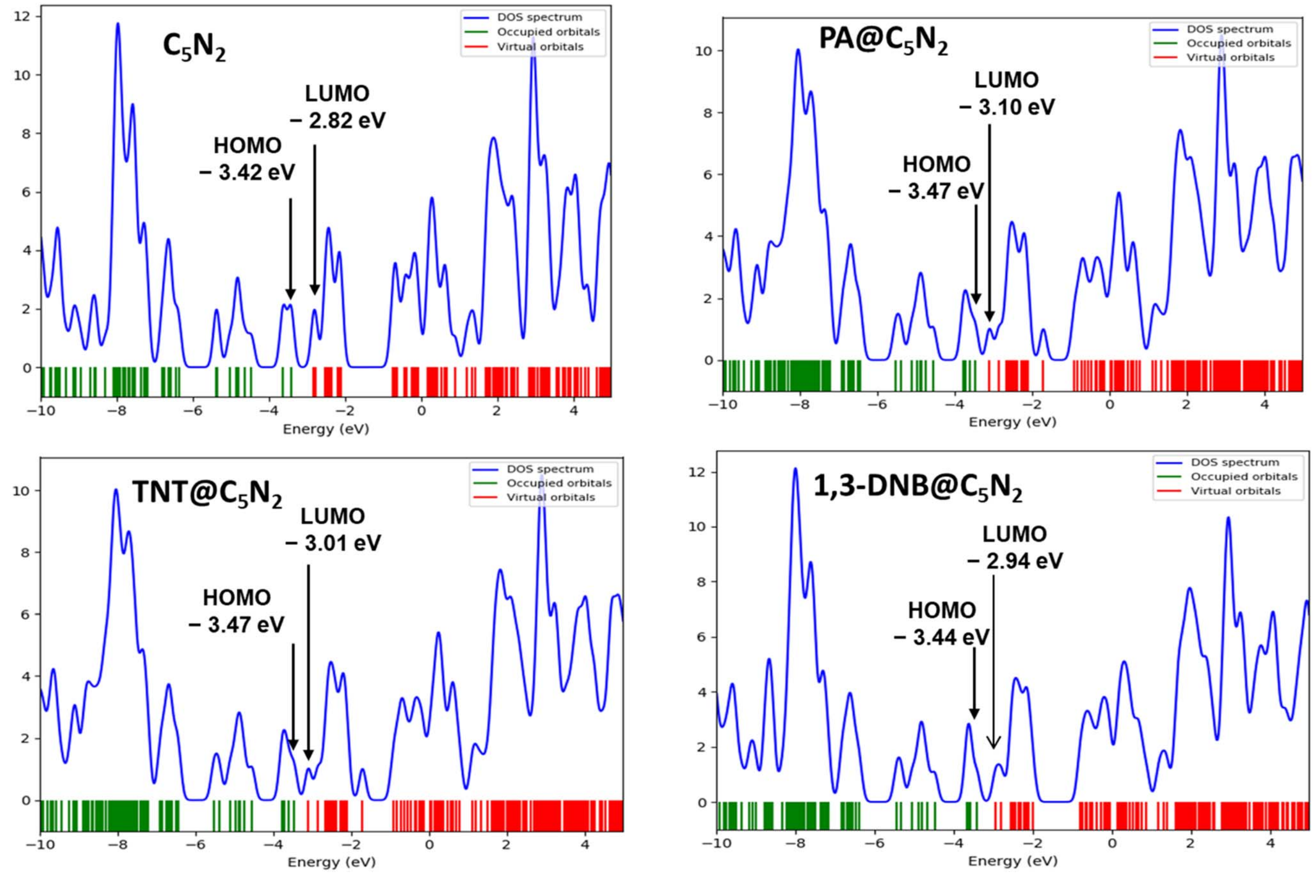

Fig. 6 DOS spectra of the pristine C_5N_2, PA@C_5N_2, TNT@C_5N_2 and 1,3-DNB@C_5N_2.

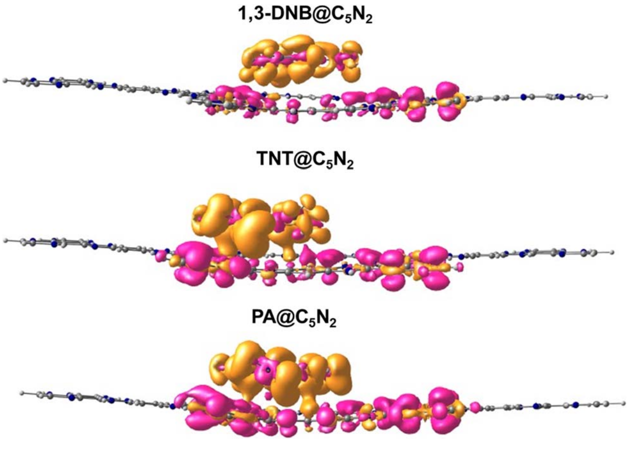

Fig. 7 EDD plots of nitroaromatics@C_5N_2 complexes. The orange color isosurface shows the charge-accumulated region and the pink color isosurface represents the charge-depleted region.

of picric acid@C_5N_2 complex, the analyte is covered primarily with orange isosurface which depicts the shifting of electron density from pyrazine and benzene ring of C_5N_2, making them depleted region shown by pink color isosurface. The orange isosurface covering the phenolic group of picric acid along with three nitro groups signifies strong extraction of electrons from the benzene ring of C_5N_2 substrate as compared to TNT@C_5N_2 and 1,3-DNB@C_5N_2. These results show consistency with NBO analysis.

3.5 Recovery time

Recovery time is one of the parameters to determine the reproducibility of C_5N_2 material as a sensor. Generally, thermal effects are applied to calculate the recovery time through transition state theory.[79] The equation for calculating recovery time is as follows:

$$\tau = \nu^{-1} e^{-E_{\text{ads}}/KT} \tag{5}$$

The τ stands for the recovery time, ν represents the attempt frequency (10^{14} s^{-1}),[45,80,81] E_{ads} express the adsorption energy, K denotes Boltzmann constant (1.99×10^{-3} kcal mol^{-1} K^{-1}), while T represents the temperature. For calculating the recovery time for the nitroaromatics@C_5N_2, different temperatures are employed. Generally, recovery time is directly proportional to interaction energies. Therefore, the recovery times for 1,3-DNB@C_5N_2, TNT@C_5N_2 and PA@C_5N_2 are, 5.24×10^{-4} s, 4.10 s and 74.74 s, respectively at 473 K. The recovery time of the nitroaromatics@C_5N_2 at different temperatures is presented in the Table S3.† It is observed that the systems' recovery time decreases with an increase in temperature.[81]

4 Conclusion

DFT calculations have been employed to determine the sensing capability of C_5N_2 substrate towards the lethal nitroaromatic compounds including 1,3-dinitrobenzene, trinitrotoluene and picric acid. Structures of nitroaromatics, C_5N_2 sheet, and their complexes have been optimised at the PBE0-D3BJ/def2SVP level of theory. Nitroaromatics are placed at five positions with different orientations to get the most stable geometry. Among studied systems, PA@C_5N_2 is observed with high interaction energy of -34.37 kcal mol^{-1}. The trend in interaction is as follows: PA@C_5N_2 > TNT@C_5N_2 > 1,3-DNB@C_5N_2. Geometrical and electronic properties are determined for better understanding of the nature and type of interactions. QTAIM and NCI analyses confirm the existence of non-covalent interactions. The presence of denser green isosurface in 3D, along with bluish-green spots in the 2D RDG graph, shows the strong non-covalent interactions in the PA@C_5N_2 complex. These NCI results are verified by small and positive values of Laplacian and electronic density obtained through topological parameters. The conductivity of C_5N_2 has been increased after the adsorption of analytes due to a reduction in the HOMO–LUMO gap. More significant change is observed for PA@C_5N_2 (0.37) which shows selectivity of C_5N_2 towards the PA. FMO results are also confirmed by DOS analysis, which shows the prominent shifting of virtual orbital after the adsorption of PA. Charge transfer (NBO) analysis also shows that among the studied systems, significant charge transfer is observed for the PA@C_5N_2 system. Furthermore, EDD analysis confirms the NBO analysis by providing visual illustrations. Recovery time for all the studied complexes has been computed using the transition state theory equation. The results of recovery time follow the interaction energies; however, recovery time could be appreciably reduced by increasing temperature. These results show that the C_5N_2 substrate could be an efficient electrochemical sensor towards toxic nitroaromatics.

Data availability

The authors confirm that the data supporting the findings of this study are available within the article [and/or] its ESI.† Any further information will also be available upon request from the authors

Conflicts of interest

There are no conflicts of interest to declare.

Acknowledgements

Computational facilities were provided by the Hope College high-performance computing cluster Curie.

References

1 D. T. McQuade, A. E. Pullen and T. M. Swager, Conjugated Polymer-Based Chemical Sensors, *Chem. Rev.*, 2000, **100**(7), 2537–2574.

2 G. Awasthi, *et al.*, Progressive Trends in Hybrid Material-Based Chemiresistive Sensors for Nitroaromatic Compounds, *Polymers*, 2022, **14**(21), 4643.

3 K. Milligan, *et al.*, Detection of Multiple Nitroaromatic Explosives via Formation of a Janowsky Complex and SERS, *Anal. Chem.*, 2020, **92**(4), 3253–3261.

4 P. Ghosh, *et al.*, Recognition of an Explosive and Mutagenic Water Pollutant, 2,4,6-Trinitrophenol, by Cost-Effective Luminescent MOFs, *Eur. J. Inorg. Chem.*, 2015, **2015**(17), 2851–2857.

5 V. Anand and V. Srivastava, Photocatalytic Degradation of Nitrobenzene and Azo Dye Using Zinc Oxide Nanoparticles Prepared by Electrochemical Method, *J. Sci. Ind. Res.*, 2016, **75**, 632–637.

6 K.-S. Ju and R. E. Parales, Nitroaromatic Compounds, from Synthesis to Biodegradation, *Microbiol. Mol. Biol. Rev.*, 2010, **74**(2), 250–272.

7 R. K. Jain, J. H. Dreisbach and J. C. Spain, Biodegradation of p-nitrophenol via 1,2,4-benzenetriol by an Arthrobacter sp, *Appl. Environ. Microbiol.*, 1994, **60**(8), 3030–3032.

8 M. Kaur, S. K. Mehta and S. K. Kansal, A fluorescent probe based on nitrogen doped graphene quantum dots for turn off sensing of explosive and detrimental water pollutant, TNP in aqueous medium, *Spectrochim. Acta, Part A*, 2017, **180**, 37–43.

9 F. Rowell, *et al.*, Detection of nitro-organic and peroxide explosives in latent fingermarks by DART- and SALDI-TOF-mass spectrometry, *Forensic Sci. Int.*, 2012, **221**(1), 84–91.

10 Q. Zhou, *et al.*, Detection of Nitro-Based and Peroxide-Based Explosives by Fast Polarity-Switchable Ion Mobility Spectrometer with Ion Focusing in Vicinity of Faraday Detector, *Sci. Rep.*, 2015, **5**(1), 10659.

11 M. Tabrizchi and V. Ilbeigi, Detection of explosives by positive corona discharge ion mobility spectrometry, *J. Hazard. Mater.*, 2010, **176**(1), 692–696.

12 A. E. Akmalov, *et al.*, A laser desorption ion-mobility increment spectrometer for detection of ultralow concentrations of nitro compounds, *Instrum. Exp. Tech.*, 2013, **56**(3), 309–316.

13 Q. Lu, *et al.*, Sensitive capillary electrophoresis microchip determination of trinitroaromatic explosives in nonaqueous electrolyte following solid phase extraction, *Anal. Chim. Acta*, 2002, **469**(2), 253–260.

14 A. Hilmi, J. H. T. Luong and A.-L. Nguyen, Development of Electrokinetic Capillary Electrophoresis Equipped with Amperometric Detection for Analysis of Explosive Compounds, *Anal. Chem.*, 1999, **71**(4), 873–878.

15 S. Singh, Sensors—An effective approach for the detection of explosives, *J. Hazard. Mater.*, 2007, **144**(1), 15–28.

16 M. Marshall and J. C. Oxley, *Aspects of Explosives Detection*, Elsevier Science, 2011.

17 A. J. Bandodkar, *et al.*, Solid-state Forensic Finger sensor for integrated sampling and detection of gunshot residue and explosives: towards 'Lab-on-a-finger', *Analyst*, 2013, **138**(18), 5288–5295.

18 L. Benny, *et al.*, Waste elimination to porous carbonaceous materials for the application of electrochemical sensors: Recent developments, *J. Cleaner Prod.*, 2021, **290**, 125759.

19 M. R. Jalali Sarvestani and Z. Doroudi, Fullerene (C20) as a potential sensor for thermal and electrochemical detection of amitriptyline: A DFT study, *J. Chem. Lett.*, 2020, **1**(2), 63–68.

20 L. E. Kreno, *et al.*, Metal–Organic Framework Materials as Chemical Sensors, *Chem. Rev.*, 2012, **112**(2), 1105–1125.

21 A. J. González Fá, R. Faccio and I. López-Corral, Detection of SOF_2 and SO_2F_2 through aluminium nitride nanosheets: A DFT study, *Appl. Surf. Sci.*, 2021, **538**, 147899.

22 S. S. Dindorkar and A. Yadav, Monolayered Silicon Carbide for Sensing Toxic Gases: a Comprehensive Study Based on the First-principle Density Functional Theory, *Silicon*, 2022, **14**(17), 11771–11779.

23 F. Li and H. Asadi, DFT study of the effect of platinum on the H_2 gas sensing performance of ZnO nanotube: Explaining the experimental observations, *J. Mol. Liq.*, 2020, **309**, 113139.

24 T. Jadoon, T. Mahmood and K. Ayub, Silver-graphene quantum dots based electrochemical sensor for trinitrotoluene and p-nitrophenol, *J. Mol. Liq.*, 2020, **306**, 112878.

25 A. S. Rad, Al-doped graphene as modified nanostructure sensor for some ether molecules: Ab-initio study, *Synth. Met.*, 2015, **209**, 419–425.

26 Y. Li, Y. Xu and X. Li, The sensing mechanism of HCHO gas sensor based on transition metal doped graphene: Insights from DFT study, *Sens. Actuators, A*, 2022, **338**, 113460.

27 H. Sajid, *et al.*, Novel microporous B_6N_6 covalent organic framework (COF) as an electrochemical sensor for the ultra-selective detection of nitroaniline isomers; a DFT outcome, *Surf. Interfaces*, 2021, **27**, 101587.

28 B. A. Farooqi, *et al.*, Graphene-polyaniline composite as superior electrochemical sensor for detection of cyano explosives, *Eur. Polym. J.*, 2020, **138**, 109981.

29 D. Sharma and T. Singh, A DFT study of polyaniline/ZnO nanocomposite as a photocatalyst for the reduction of methylene blue dye, *J. Mol. Liq.*, 2019, **293**, 111528.

30 M. F. Fellah, Pt doped (8,0) single wall carbon nanotube as hydrogen sensor: A density functional theory study, *Int. J. Hydrogen Energy*, 2019, **44**(49), 27010–27021.

31 U. Kumar and B. C. Yadav, Development of humidity sensor using modified curved MWCNT based thin film with DFT calculations, *Sens. Actuators, B*, 2019, **288**, 399–407.

32 A. S. Rad, *et al.*, Ab-initio study of interaction of some atmospheric gases (SO_2, NH_3, H_2O, CO, CH_4 and CO_2) with polypyrrole (3PPy) gas sensor: DFT calculations, *Sens. Actuators, B*, 2015, **220**, 641–651.

33 M. Noei, Different electronic sensitivity of BN and AlN nanoclusters to SO_2 gas: DFT studies, *Vacuum*, 2017, **135**, 44–49.

34 T. Wang, *et al.*, A Review on Graphene-Based Gas/Vapor Sensors with Unique Properties and Potential Applications, *Nano-Micro Lett.*, 2016, **8**(2), 95–119.

35 F. K. Kessler, *et al.*, Functional carbon nitride materials — design strategies for electrochemical devices, *Nat. Rev. Mater.*, 2017, **2**(6), 17030.

36 G. Zhang, *et al.*, Overall water splitting by Pt/gC 3 N 4 photocatalysts without using sacrificial agents, *Chem. Sci.*, 2016, **7**(5), 3062–3066.

37 L. Tan, *et al.*, Novel two-dimensional crystalline carbon nitrides beyond gC_3N_4: structure and applications, *J. Mater. Chem. A*, 2021, **9**(1), 17–33.

38 M. Yar, M. A. Hashmi and K. Ayub, Nitrogenated holey graphene (C_2N) surface as highly selective electrochemical sensor for ammonia, *J. Mol. Liq.*, 2019, **296**, 111929.

39 M. Asif, *et al.*, A first principles study on electrochemical sensing of highly toxic pesticides by using porous C_4N nanoflake, *J. Phys. Chem. Solids*, 2022, **160**, 110345.

40 M. Yar, M. A. Hashmi and K. Ayub, The C_2N surface as a highly selective sensor for the detection of nitrogen iodide from a mixture of NX_3 (X= Cl, Br, I) explosives, *RSC Adv.*, 2020, **10**(53), 31997–32010.

41 S. Qureshi, *et al.*, First-principles study for electrochemical sensing of neurotoxin hydrazine derivatives via h-g-C_3N_4 quantum dot, *Surf. Interfaces*, 2022, **30**, 101913.

42 S. Qureshi, *et al.*, Electrochemical sensing of heptazine graphitic C_3N_4 quantum dot for chemical warfare agents; a quantum chemical approach, *Mater. Sci. Semicond. Process.*, 2022, **148**, 106753.

43 M. Yar, *et al.*, Adsorption and sensor applications of C_2N surface for G-series and mustard series chemical warfare agents, *Microporous Mesoporous Mater.*, 2021, **317**, 110984.

44 S. Sarfaraz, *et al.*, DFT investigation of adsorption of nitro-explosives over C_2N surface: Highly selective towards trinitro benzene, *J. Mol. Liq.*, 2022, **352**, 118652.

45 M. Yar, *et al.*, Selective detection and removal of picric acid by C2N surface from a mixture of nitro-explosives, *New J. Chem.*, 2020, **44**(43), 18646–18655.

46 Y. Kou, *et al.*, Supercapacitive Energy Storage and Electric Power Supply Using an Aza-Fused π-Conjugated Microporous Framework, *Angew. Chem., Int. Ed.*, 2011, **50**(37), 8753–8757.

47 S. Kim and H. C. Choi, Light-promoted synthesis of highly-conjugated crystalline covalent organic framework, *Commun. Chem.*, 2019, **2**(1), 60.

48 Y. Cao, *et al.*, Hydrogen peroxide synthesis on porous graphitic carbon nitride using water as a hydrogen source, *J. Mater. Chem. A*, 2020, **8**(1), 124–137.

49 Z.-D. Yang, W. Wu and X. C. Zeng, Electronic and transport properties of porous graphenes: two-dimensional benzo-and aza-fused π-conjugated-microporous-polymer sheets and boron–nitrogen co-doped derivatives, *J. Mater. Chem. C*, 2014, **2**(16), 2902–2907.

50 M. J. Frisch, G. W. Trucks, H. B. Schlegel, G. E. Scuseria, M. A. Robb, J. R. Cheeseman, *et al.*, *Gaussian 16, Revision C. 01.* 2016.

51 A. Yaghoubi and A. Ramazani, Using Gaussian and GaussView software for effective teaching of chemistry by drawing molecules, *Res. Chem. Educ.*, 2024, **6**(1), 69–90.

52 C. Adamo and V. Barone, Toward reliable density functional methods without adjustable parameters: The PBE0 model, *J. Chem. Phys.*, 1999, **110**(13), 6158–6170.

53 M. Ibarra-Rodríguez, P. Horley and M. Sánchez, Metal-adorned borophene for efficient glucose adsorption, *Comput. Theor. Chem.*, 2024, **1231**, 114403.

54 H. Louis, *et al.*, Modeling of Mg12O11–X (X = B, N, P and S) Nanostructured Materials as Sensors for Melamine (C3H6N6), *J. Comput. Biophys. Chem.*, 2022, **21**(08), 999–1021.

55 M. Ibarra-Rodríguez and M. Sánchez, Graphitic carbon nitride functionalized with four boron atoms for adsorption and separation of CO2/CH4: DFT calculations, *Adsorption*, 2020, **26**(4), 597–605.

56 M. Ibarra-Rodríguez and M. Sánchez, Adsorption of metformin on graphitic carbon nitride functionalized with metals of group 1–3 (Li, Na, K, Be, Mg, Ca, B, Al, and Ga), DFT calculations, *Comput. Theor. Chem.*, 2022, **1207**, 113532.

57 M. Ibarra-Rodríguez and M. Sánchez, Adsorption of H2, N2, CO, H2S, NH3, SO2 and CH4 on Li-functionalized graphitic carbon nitride investigated by density functional theory, *Bull. Mater. Sci.*, 2020, **43**(1), 144.

58 L. F. Paredes-Pérez, *et al.*, Guanidinium and spermidinium decavanadates: as small biomimetic models to understand non-covalent interactions between decavanadate and arginine and lysine side chains in proteins, *Front. Chem. Biol.*, 2024, **3**, 1451167.

59 F. A. Nelson, *et al.*, The iron group transition-metal (Fe, Ru, Os) coordination of Se-doped graphitic carbon (Se@ gC 3 N 4) nanostructures for the smart therapeutic delivery of zidovudine (ZVD) as an antiretroviral drug: a theoretical calculation perspective, *RSC Adv.*, 2023, **13**(48), 34078–34096.

60 L. Yang, *et al.*, DFT-D3 and TD-DFT studies on the sensor performance of the functionalized carbon quantum dots for curcumin, *Surf. Interfaces*, 2024, **45**, 103870.

61 K. Wu, *et al.*, Multifunctional semiconducting carbon nitrides enabling sequential fluorescent sensing of telomerase activity and internal self-checking, *Sens. Actuators, B*, 2023, **378**, 133170.

62 S. Grimme, Semiempirical GGA-type density functional constructed with a long-range dispersion correction, *J. Comput. Chem.*, 2006, **27**(15), 1787–1799.

63 S. Grimme, *et al.*, A consistent and accurate ab initio parametrization of density functional dispersion correction (DFT-D) for the 94 elements H-Pu, *J. Chem. Phys.*, 2010, **132**(15), 154104.

64 T. Lu and F. Chen, Multiwfn: A multifunctional wavefunction analyzer, *J. Comput. Chem.*, 2012, **33**(5), 580–592.

65 W. Humphrey, A. Dalke and K. Schulten, VMD: Visual molecular dynamics, *J. Mol. Graphics*, 1996, **14**(1), 33–38.

66 C. Legault, *CYLview, 1.0b*, Université de Sherbrooke Canada, 2009.

67 S. Pan, *et al.*, Selectivity in Gas Adsorption by Molecular Cucurbit[6]uril, *J. Phys. Chem. C*, 2016, **120**(26), 13911–13921.

68 T. Lu and F. Chen, Bond Order Analysis Based on the Laplacian of Electron Density in Fuzzy Overlap Space, *J. Phys. Chem. A*, 2013, **117**(14), 3100–3108.

69 N. S. Venkataramanan, A. Suvitha and Y. Kawazoe, Unravelling the nature of binding of cubane and substituted cubanes within cucurbiturils: A DFT and NCI study, *J. Mol. Liq.*, 2018, **260**, 18–29.

70 S. A. Bhadane, D. N. Lande and S. P. Gejji, Understanding Binding of Cyano-Adamantyl Derivatives to Pillar[6]arene Macrocycle from Density Functional Theory, *J. Phys. Chem. A*, 2016, **120**(43), 8738–8749.

71 N. L. Marana, S. M. Casassa and J. R. Sambrano, Adsorption of NH3 with Different Coverages on Single-Walled ZnO Nanotube: DFT and QTAIM Study, *J. Phys. Chem. C*, 2017, **121**(14), 8109–8119.

72 M. Aetizaz, S. Sarfaraz and K. Ayub, Interaction of imidazolium based ionic liquid electrolytes with carbon nitride electrodes in supercapacitors; a step forward for understanding electrode–electrolyte interaction, *J. Mol. Liq.*, 2023, **369**, 120955.

73 D. Cremer and E. Kraka, Chemical Bonds without Bonding Electron Density — Does the Difference Electron-Density Analysis Suffice for a Description of the Chemical Bond?, *Angew Chem. Int. Ed. Engl.*, 1984, **23**(8), 627–628.

74 G. Zhurko, *Chemcraft*, 2014, vol. 22, https://www.chemcraftprog.com.

75 W.-j. Hu, *et al.*, Theoretical investigation on the intermolecular interactions between 3-nitro-1,2,4-triazol-5-one and 2,6-diamino-3,5-dinitropyrazine-1-oxide using DFT methods, *Chem. Pap.*, 2022, **76**(5), 2747–2758.

76 H. Sajid, *et al.*, Effective adsorption of A-series chemical warfare agents on graphdiyne nanoflake: a DFT study, *J. Mol. Model.*, 2021, **27**(4), 117.

77 H. Sajid, *et al.*, High selectivity of cyclic tetrapyrrole over tetrafuran and tetrathiophene toward toxic chemicals; A first-principles study, *Microporous Mesoporous Mater.*, 2020, **299**, 110126.

78 A. S. Rad and K. Ayub, O3 and SO2 sensing concept on extended surface of B12N12 nanocages modified by Nickel decoration: A comprehensive DFT study, *Solid State Sci.*, 2017, **69**, 22–30.

79 M. Rakib Hossain, *et al.*, First-principles study of the adsorption of chlormethine anticancer drug on C24, B12N12 and B12C6N6 nanocages, *Comput. Theor. Chem.*, 2021, **1197**, 113156.

80 Z. Zhao, *et al.*, Gas-Sensing Properties of the SiC Monolayer and Bilayer: A Density Functional Theory Study, *ACS Omega*, 2020, **5**(21), 12364–12373.

81 S. Peng, *et al.*, Ab initio study of CNT NO2 gas sensor, *Chem. Phys. Lett.*, 2004, **387**(4), 271–276.